

**NON-CRYSTALLINE OXIDES AND CHALCOGENIDES: A NEW PARADIGM
BASED ON *AB INITIO* QUANTUM CHEMISTRY CALCULATIONS FOR
SHORT RANGE ORDER AND PROPERTIES, AND BOND-CONSTRAINT
THEORY FOR NETWORK CONNECTIVITY, NETWORK DISRUPTION
AND CHEMICAL PHASE SEPARATION**

G. Lucovsky*

Department of Physics, NC State University, Campus Box 8202, Raleigh,
NC 27695-8202, USA

The bonding and properties of non-crystalline chalcogenide glasses and thin films are compared with those of non-crystalline bulk glass and thin film oxides. This approach provides a methodology for understanding some of the more important applications of chalcogenides in the context of significant qualitative similarities and quantitative differences between these two classes of technologically important non-crystalline solids. The theoretical foundation for comparisons is two-fold: i) *ab initio* quantum chemistry calculations on small clusters to study short range order and properties dependent of this scale of order, and ii) bond constraint theory of identify the effects of network connectivity and bonding constraints. This approach is first applied to infrared effect charges and differences in the photo-structural network response between As_2S_3 and GeS_2 . The methodology is then extended to comparisons between thin film silicate alloys, and their chalcogenide counter-parts, with emphasis on understanding the broader range of reversible memory and transport behaviors in the chalcogenide films and glasses. Finally, self-organization is addressed in oxide and chalcogenide thin films, providing the basis for device applications. These include ternary silicate alloys with irreversible self-organizations that are enabling for gate dielectrics, as well reversible self organizations in $GeTe-Sb_2Se_3$ alloys for information storage in read/write optical memories.

(Received May 19, 2005; accepted July 21, 2005)

Keywords: Continuous random networks, Chalcogenide alloys, SiO_2 alloys, Silicates, *Ab initio* calculations, Bond constraint theory, Floppy and stressed-rigid films, Intermediate phases, Network disruption and modification, Chemical phase separation

1. Introduction

A major distinction and disconnect has evolved in the field of non-crystalline solids between experimental and theoretical studies of oxides and chalcogenides, primarily due to differences in the respective materials that have been exploited in important applications. Many of the more significant applications of oxides have been in bulk glass silicate alloys with control of the index of refraction for optical components being one of the more important areas addressed. The evolution of microelectronics has broadened the applications of oxides significantly, including thermally-grown SiO_2 as a gate dielectric, and thin film SiO_2 alloys with silicon nitride (Si_3N_4), P_2O_5 and B_2O_3 playing important roles in the evolution of integrated circuit technology. Advanced microelectronic applications have recently focused on transition metal (TM) and lanthanide rare earth (RE) atom oxides as replacement dielectrics for thermally grown SiO_2 .

In marked contrast, many of the important applications of the chalcogenides have either been in thin film or thick film structures that involve photo-conducting or semiconducting properties, and more recently reversible bonding transitions that are important for information storage and manipulation.

This article will not attempt to provide a comprehensive survey of applications and

* Corresponding author: lucovsky@ncsu.edu

materials, but instead will attempt to bridge the disconnect that has evolved, and point out how increased understanding can be obtained from addressing qualitative similarities in properties and technology enabling effects, as well as quantitative differences.

The comparisons addressed in this article will build on two different aspects of theory: i) *ab initio* quantum chemistry calculations using small clusters that include the elements of short range order obtained from diffraction studies [1], and ii) bond constraint theory, BCT, that establishes significant aspects of network connectivity, and either floppy, intermediate phase or stressed-rigid bonding that are important in enabling device applications [2,3,4,5].

2. *Ab initio* calculations: SiO₂ and transition metal oxides

The *ab initio* calculations highlighted in this article were first applied to SiO₂ [1], using the cluster in Fig. 1(a) that includes the Si-O, and Si-Si and O-O bond lengths (or equivalently the Si-O-Si and O-Si-O bond angles) obtained from diffraction studies [6,7]. This is an excellent test of the method since there is relatively new diffraction data with regard to bond-angle distributions that can be directly compared with the calculations [8,9]. These comparisons are a more stringent test of the theoretical approach than similar comparisons for the more covalent chalcogenide glasses and films such as As₂S₃ and GeS₂ that are the primary focus of the article.

The 9-atom Si-O clusters of Fig. 1(a) are terminated either by i) Si* pseudo-atoms that preserve Si and O core levels, and dipole moments, or ii) H-atoms with essentially equivalent results. The *ab initio* calculations give an average Si-O-Si bond angle of $148 \pm 2^\circ$, and a bond angle distribution of $\sim 19^\circ \pm 2^\circ$ in good agreement with recently published results [8,9]. This distribution is significantly different from the $>30^\circ$ bond angle spread of Mozzi and Warren [6]. The same method, applied to GeO₂, BeF₂, GeS₂ and As₂S₃, gives values of ground state properties in excellent agreement with experiment, including i) the average bond angles and bond angle distributions, and ii) the infrared effective charges for the normal mode infrared vibrations [10].

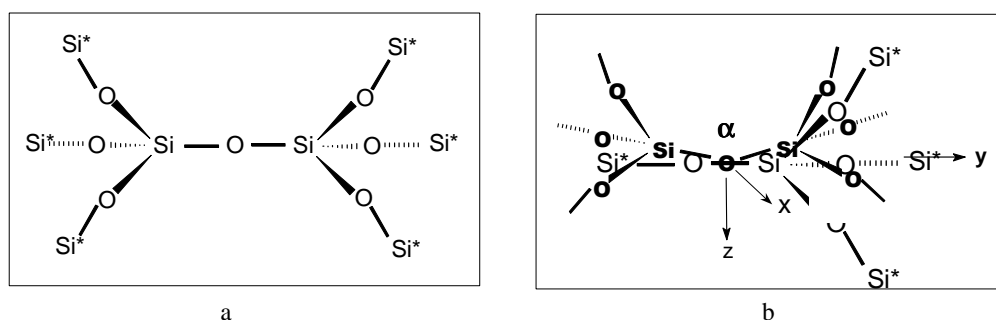


Fig. 1. (a) Schematic representation of the Si-O-Si terminated cluster used for the *ab-initio* calculations of this paper. The Si-O-Si bond angle, α , is 180° in this diagram, and will be varied from 120° to 150° for the calculations. The Si* represent an embedding potential that Si core eigenvalues are correct. (b) Normal mode motions in non-crystalline SiO₂.

The electronic structure calculations employ variational methods in which an exact Hamiltonian is used, and are done initially at a self-consistent field (SCF) Hartree-Fock level with a single determinant wave function that does not include electron correlation. Following this, there is a configuration interaction (CI) refinement of the molecular orbitals based on a multi-determinant expansion of the wave function including electron correlation [1]. Based on the variational principle any increase in binding energy based on the CI refinement provides an improved solution to the calculation.

Fig. 2 presents the dependence of the total energy for SiO₂ as a function of the bond angle of the two-fold coordinated O-atom for a constant Si-Si distance of ~ 0.31 nm [11]. The ground state energy distribution is relatively insensitive to the dihedral angles that define the orientation of the terminating groups. More importantly, the results emphasize the importance of contributions with d-like symmetries to the Si basis set. These are equally important for Ge, S, and F, and have been included in the respective calculations [10]. It is significant to note that the calculated minimum in total energy occurs at a Si-O-Si bond angle of $148 \pm 2^\circ$ and is different than the 144° bond angle in Ref. 6 and 7, but approximately equal to the average bond angle determined for SiO₂ in Refs. 8 and 9.

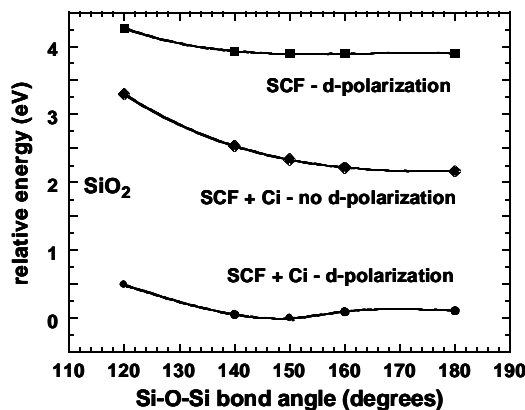


Fig. 2. Calculated energy in eV as a function of the Si-O-Si bond angle for SCF with d polarization, SCF + CI (no d polarization), and SCF + CI + d polarization.

The IR effective charges, e_{Tj} , $j = AS, SS$ and R , have been calculated for the asymmetric bond-stretching (AS), v_y , symmetric bond-stretching or (bond-bending) (SS or B), v_z , and out-of-plane bond-rocking (R), v_x , infrared active vibrations of non-crystalline SiO_2 [10]. Similar calculations have been made for the GeO_2 , BeF_2 , GeS_2 , as well as As_2S_3 . $e_{Tj} = \Delta\mu_{\phi}/q_j s$, where $\Delta\mu_{\phi}$ the change in the dipole moment for the i^{th} normal mode displacement Δq_j . The three orthogonal normal mode motions of O-atoms are defined with respect to the coordinate system displayed in Fig. 1(b). The normal coordinate is y for the asymmetric (AS) bond-stretching vibration, and the relative motion of the O-atom is parallel to a line joining the neighboring Si-atom. The normal coordinate is z for the symmetric (SS) bond-stretching vibration, and the relative motion of the O-atom is in the direction of the bisector of the Si-O-Si bond angle, α . Finally, the normal coordinate is x bond-rocking (R) vibration, and is perpendicular to the plane of the Si-O-Si bonding group. The IR effective charges have been calculated from SCF and CI calculations as a function of α . The displacements Δx , Δy and Δz for the calculations were $<5\%$ of a nominal Si-O bond length of 0.16 nm. There are two contributions to the effective charges, one from the equilibrium charge distribution, e_E , and the second from dynamic charge redistributions, e_{CR} , that occur during the normal mode motions [1,12]; total effective charge, $e_{Tj} = e_{Ej} + e_{CRj}$ [1,10]. These e_{Tj} values are approximately the same for SiO_2 and GeO_2 , and for GeS_2 and As_2S_3 , and agreement with experiment is excellent for SiO_2 , GeS_2 and As_2S_3 . Additionally, i) the ratios of the IR dielectric functions for GeO_2 are also in agreement with the calculated effective charges [13], and ii) the effective charge for the symmetric stretching mode in BeF_2 cannot be detected by reflectivity in agreement with its very low value [14].

The same method has been applied to transition metal (TM) elemental oxides that have been proposed as alternative gate dielectrics for advanced Si devices [15]. These calculations have focused primarily on the TM d-states that contribute to the lowest energy conduction band electronic structure. Figure 3 summarize the results of these calculations, indicating the evolution of these d-state term splittings for a i) centro-symmetry bonding environment, as in a non-crystalline thin film, ii) distorted bonding as in tetragonal and orthorhombic crystalline phases, and iii) at grain boundaries in nanocrystalline thin films. Changes in band edge states have been used to detect the transition from non-crystalline Zr-O bonding in silicate alloy to crystalline bonding in a chemically separated ZrO_2 phase [16].

3. Bond constraint theory (BCT)

Three aspects of BCT are summarized: i) the determination of mean field coordination, n_c , and bonding constraints per atom, r_c , initially also designated as N_{av} and C_{av} , respectively [2,3], ii) the intermediate phase as applied to continuous random network structures, CRNs [4,5], and iii) the extension of bond-constraint theory to silicate and chalcogenide alloys in which the introduction of ionic alloy constituents promotes network disruption and modification [17].

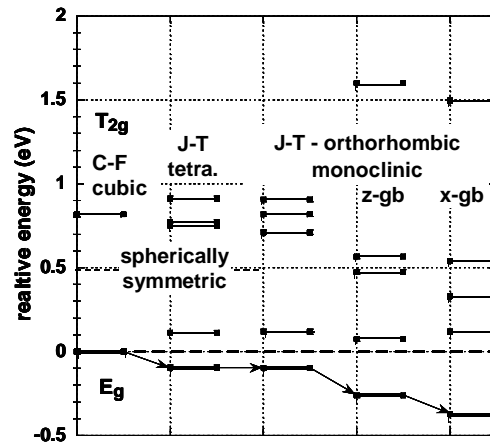


Fig 3. Calculated conduction band edge d-states for $Zr(Hf)O_2$. The crystal field (C-F) splitting into a T_{2g} triplet and an E_g doublet state are for an undistorted cubic arrangement of eight of O neighbors. The Jahn-Teller (J-T) distortions associated respectively with orthorhombic and monoclinic eight-neighbor distortions, and finally, there are additional J-T term-splittings associated with representative grain boundary distortions.

Consider first n_c and r_c . These concepts were first applied to covalent-bonded continuous random networks, CRNs in which the constituent atoms are two-, three- or four-fold coordinated, and the three- and four-fold coordinated atoms were in non-planar arrangements [2,3]. The mean-field coordination, or equivalently the number of bonds per atom was obtained by applying the 8-N rule for bonding counting, and proceeding accordingly [17]. The number of bond-stretching constraints/atom $n_c]_{stretch}$ is given by $m/2$ where m is the bonding coordination, and the number of bending constraints/atom, $n_c]_{bend}$ is given by $2m-3$. This leads to the first important result regarding the number of bonding constraints/atom:

$$r_c(C_{av}) = 2.5 n_c(N_{av}) - 3. \quad [1]$$

Bonding of in planar arrangements reduces the number of bond bending constraints/atom to $m-1$, so that r_c is modified accordingly. Applied to Si_3N_4 , in which N is three-fold coordinated and in a planar bonding arrangement. This reduces the number of bond bending constraints from $2m-3 = 3$ to $m-1 = 2$. Since the number of planar N atoms is $n = 4$, and the total number of atoms in the molecular representation is $N_T = 7$, r_c is given by

$$r_c = 2.5 n_c - 3 - 0.4 n/N_T. \quad [2]$$

The number of bonding constraints, r_c is then equal to 5.35, and is reduced from 5.58 before this correction was made. For two fold coordinated atoms, $2m-3 = m-1$, so that the counting is unchanged. Finally for terminal atoms, $m-1 = 0$, and there are no bond bending constraints [4,5].

For all of the examples that follow the mean field condition for the onset of stressed-rigid networks is $r_c = 2.4$, corresponding to a value of $n_c = 3$, the dimensionality of the network. In the mean-field approximation this value of r_c separates a floppy or under-constrained alloy composition range, as in Ge_xSe_{1-x} , with $x = 0.2$ from an over-constrained or stressed-rigid regime of alloy compositions [4,5]. However, as has been demonstrated in Refs. 4, 5 and 18 that there is generally an intermediate phase regime that delays the onset of global rigidity through a chemical bonding self-organization [4,5]. This prevents the percolation of bond-strain until $r_c \sim 2.52$, so that there are two-transitions, instead of one as predicted by Maxwellian or mean-field theory. The first transition marks the onset of local bonding rigidity, and the percolation of bonding rigidity. The intermediate phase regime displays some remarkable properties with regard to glasses, and/or thin films in the floppy and stressed-rigid regimes that bracket it. For example, there is reversibility of heat flow as contrasted with irreversible heat flow in the both the floppy and stressed-rigid regimes [4,5].

4. Ab Initio and bond constraint theory and vibrational spectroscopy

The fundamental absorption features in the infra-red spectrum of SiO₂ thin films and bulk glasses are similar, and a spectrum is included in Fig. 4(a) for a thin film subjected to annealing at 900 °C in an inert gas ambient, and thereby densified [19]. The features at 450 cm⁻¹, 810 cm⁻¹ and 1075 cm⁻¹ are respectively the bond-rocking (R), symmetric stretching (SS) or bond-bending (B), and asymmetric stretching modes (AS) for which IR effective charges have been determined in Section 3. The Si and O terminating atoms to the cluster in Fig. 1(a) do not contribute directly to the IR effective charges or the displacements of the O-atoms and the effective or renormalized valence forces that have been applied to the model calculation [1]. The spectrum shows an additional feature that appears as a prominent shoulder on the high energy side of the AS feature and indicated by the arrow in Fig. 4(a). This was erroneously assigned to a longitudinal optical mode feature in Ref. 13; this assignment has been corrected [20]. This spectral feature is a direct result of network connectivity and is implicit in BCT, i.e., a network connectivity feature, NCF.

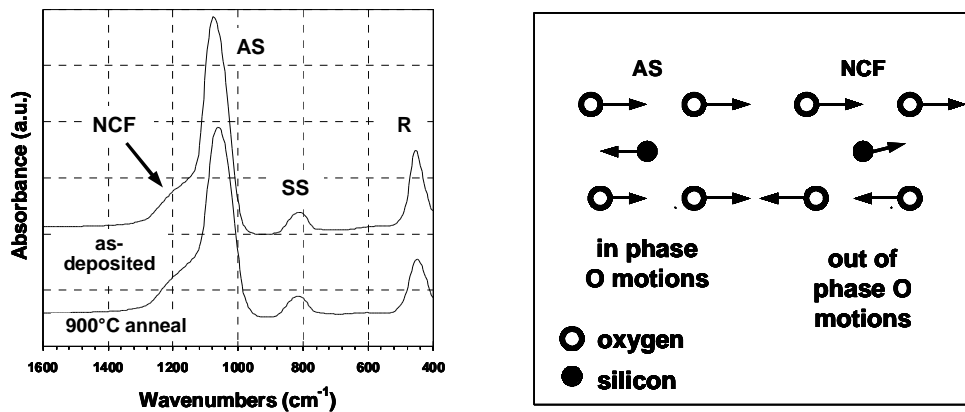


Fig. 4. (a) Upper trace: infrared absorption spectra for as-deposited (300°C) SiO₂, and lower trace: the same spectrum after annealing at 900 °C in an inert ambient. The absorptions associated with normal mode oxygen atom motions are label AS, SS and R following the notations in the text. The feature introduced by network connectivity is labeled NCF. (b) In phase and out of phase of phase atomic motions for the SA and NCF modes in (a).

The local bonding environment in Fig. 1(b) is connected to the network through four-fold coordinated Si atoms, and these are terminated by O-atoms and Si pseudo-atoms. The atomic displacements of this additional feature have been identified in Ref. 20 which employed a Cluster Bethe Lattice (CBL) method to couple local bonding displacements of the O-atom normal modes to the rest of the network structure, emulated in this example by the CBL termination. Analysis of the results for the vibrational spectrum of GeO₂ that is essentially the same as SiO₂ with respect to the normal mode motions of the O-atoms, The CBL density of state features for the O-atom motions include in-phase and out-of-phase motions. This is illustrated in Fig. 4(b) for the SS vibration, where the O-atoms move in the same directions for the in-phase motions, and the Si-atom motions are oppositely direction. In contrast, two pairs of O-atoms move in opposite directions for the out-of-phase motion, and because of the random character of the network, there are small displacements of the Si-atoms that provide the dipole moment changes for IR activity. These motions are anticipated in BCT by the constraint counting procedure that includes two bond-stretching and five bond-bending constraints for each Si atom neighbors to the O atom at the center of the cluster. In this context, BCT plays the same role in non-crystalline network solids that periodicity plays in crystals.

The vibrational spectra for GeS₂ and GeSe₂ display three features for the R, SS and AS modes have been assigned to the corresponding S- and Se-atom motions as for O-atoms in SiO₂. However, the ratio of the atomic displacements for S- and Se- atoms relative to Ge-atom displacements is different because of atomic mass ratios. In addition, the Raman spectrum of GeSe₂ indicates an additional IR feature that has been assigned to edge connectivity of GeSe_{4/2} tetrahedra [20]. The SiO_{4/2} tetrahedra are corner connected in non-crystalline and crystalline SiO₂, while the SiSe_{4/2} tetrahedra of non-crystalline and crystalline SiSe₂ are edge-connected [4,5]. This deviation

from the edge connectivity is not anticipated in BCT, and must be addressed through calculations that address both bonding environments as in Ref. 20. This aspect of chalcogenide atom bonding is not addressed in any of the examples addressed in the remainder of this article and the reader is referred to review papers by Boolchand and coworkers for more detailed discussions [4,5].

5. Photo-darkening and photo-structural changes

The ab initio calculations have been used to determine the ground state energy, and the lowest excited singlet state for band edge transitions in As_2S_3 , GeS_2 and GeO_2 that are important in reversible photo-darkening and photo-structural changes [21,22,23]. The CI refinements give better solutions for the electronic structure, and this is particularly important for the lowest excited states where there are significant changes in the local bonding, e.g., bond angle increases at the S-sites $\sim 5\text{-}10^\circ$ in As_2S_3 and GeS_2 [24].

Fig. 5 is molecular orbital energy diagram for As_2S_3 that includes the energy of the singlet band gap transition in the annealed state, and after a photo-darkening light exposure. The minima in the ground and excited singlet states for As_2S_3 are displaced by approximately 7° in the As-S-As bond-angle. In addition, and not shown in the Fig. 5, there is rotation of the AsS_2 terminal cluster groups in the excited state that is essentially the same as that described in Ref. 25, which models changes in local structure by EXAFS before and after photo-darkening. The displacement of the minima in the ground and excited states of GeS_2 is slightly larger, $\sim 10^\circ$, but no change in the relative dihedral angles for the orientation of the GeS_3 terminal cluster groups is required to optimize final state energies. The calculated singlet excitation energy for the As_2S_3 cluster differs by less than 0.5 eV from the experimental defined E_{04} band gap (energy at which the absorption constant, $\alpha_s = 10^4 \text{ cm}^{-1}$), and the agreement between the energy difference of $\sim 0.35 \text{ eV}$ for the vertical transitions of the ground and photo-induced structurally-altered states in Fig. 5, and the photo-darkening band edge shift is also very good.

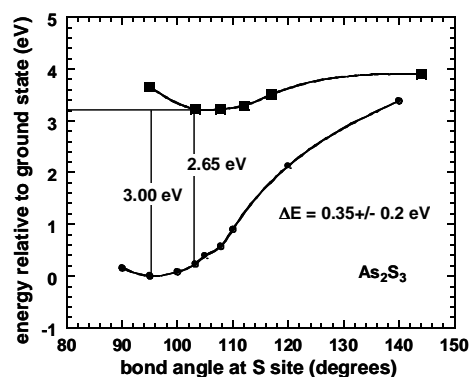


Fig. 5. Energy versus bond angle for the singlet ground state and first excited states for As_2S_3 . The energies of the electronic transitions corresponding to the effective band edges in the pristine and photo-darkened states are indicated, along with the difference in these in energies. The uncertainties of $\pm 0.3 \text{ eV}$ for the energy shift As_2S_3 is based on uncertainties of approximately $\pm 0.2 \text{ eV}$ in the energy differences between the ground and excited states.

The agreement between the calculated excitation energies, and their difference for GeS_2 is not as good as for As_2S_3 , and this may be due in part to differences in local bond strain not specifically incorporated into the cluster model. As_2S_3 is an ideal glass former, or equivalently it is at the boundary for the onset of self-organization in the As-S binary alloy system, whilst the GeS_2 composition (33% Ge) is stressed-rigid and well removed from the Ge-Se alloy intermediate phase regime [5].

Finally, the bond angle variations for GeO_2 in the ground and excited states suggest a significantly reduced band edge difference of at most 0.1 eV, so that photo-darkening is not expected to be observable. Similar considerations apply to As_2O_3 , where reversible photo-structural changes have not been reported [26].

For As_2S_3 , the photo-structural changes following light-soaking [21] do not require intra-

molecular bond scission in agreement with the model of Ref. 22, and the bond and dihedral angle changes are effectively equivalent to the inter-molecular bond scission of Ref. 22. These elastic and completely reversible photo-structural changes are consistent with the idealicity of the network structure of As_2S_3 as quantified by an average number of bonds/atom, $n_c = 2.4$, and more importantly by the average number of bonding constraints/atom, $r_c = 3$, equaling the dimensionality of the network, or atomic degrees of freedom [2-5]. As such As_2S_3 is in a regime of As-S alloy compositions in which self-organization after annealing produces strain free glasses or thin films, and aging, or equivalently photon induced intra-molecular bond scission does not occur [4,5].

The ab initio calculations for GeS_2 identify a similar initiating optical excitation for photo-darkening, but the bond scission mechanism is qualitatively different as a result of significant local bond stress. This is consistent with an increased value of n_c , 2.67 bonds/atom, and an average number of bonding constraints/atom, 3.67, that is greater than the network dimensionality of 3. Following the arguments of Refs. 4 and 5, this makes the GeS_2 network locally stressed-rigid, and qualitatively different than that of the unstressed or optimally constrained network of As_2S_3 . It also makes it energetically favorable to relieve the additional bond strain associated with photo-induced bond angle changes through intra-molecular bond scission, rather than through elastic deformations as in As_2S_3 , consistent the universal bond scission model [23].

6. Silicate and chalcogenide alloys

6.1 Zr silicate pseudo-binary and -ternary alloys

The first part of this section addresses Zr silicate pseudo-binary alloys, $(\text{ZrO}_2)_x(\text{SiO}_2)_{1-x}$, and the second Zr silicate pseudo-ternary alloys that include Si_3N_4 as well, i.e. $(\text{ZrO}_2)_x(\text{SiO}_2)_y(\text{Si}_3\text{N}_4)_{1-x-y}$. Figures 6(a) and (b) present FTIR results for Zr silicate alloys with ZrO_2 fractions, x , equal to 0.23 and 0.5 [19]. The feature at $\sim 950 \text{ cm}^{-1}$ in Fig. 6(a) for the as-deposited films is assigned to a terminal $\text{Si-O}^{\cdot-}$ group, an indicator of network disruption by addition of the ionic ZrO_2 elemental oxide into the SiO_2 host network. The broader Si-O bond-stretching feature in Fig. 6(b) is assigned to the SiO_4^{4-} molecular ion, and indicates complete network disruption in the as-deposited film, and additionally in as-deposited Zr silicate films with higher ZrO_2 compositions, i.e., $x > 0.5$. There are significant changes in FTIR spectral features in Figs. 6(a) and (b) between the as-deposited films and films annealed at $900 \text{ }^\circ\text{C}$, as well as continuous changes at intermediate annealing temperatures. The $900 \text{ }^\circ\text{C}$ changes are indicative of a chemical phase separation, CPS, into SiO_2 and ZrO_2 . This separation has been confirmed by high-resolution transmission electron microscopy, HRTEM, imaging [27]. The FTIR spectral features change continuously over the entire range of annealing temperatures indicating bonding changes that are precursors to the CPS process that is evident after the $900 \text{ }^\circ\text{C}$ anneal.

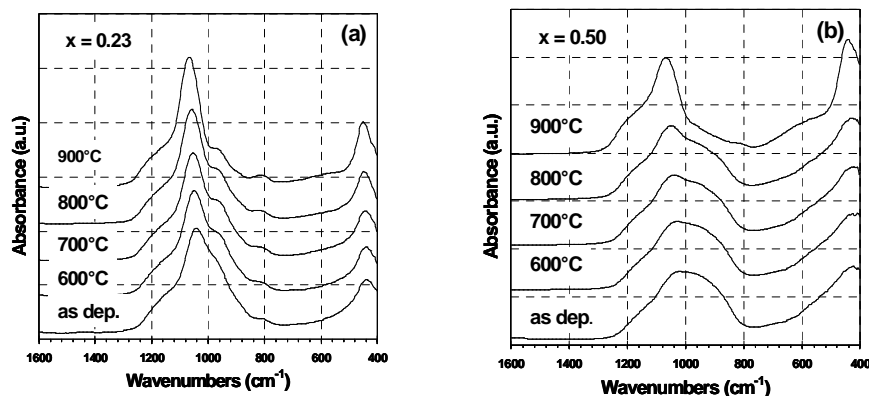


Fig. 6. Infrared absorption spectra for as-deposited and annealed Zr silicate thin films with ZrO_2 concentrations: (a) $x = 0.23$, and (b) $x = 0.50$.

There is no XRD detectable crystallization, except for the $x = 0.5$ sample after a $900 \text{ }^\circ\text{C}$ anneal; however, this is anticipated in alloys with $x > 0.5$ as well. For example, the FTIR spectra for a Zr silicate alloy with $x = 0.61$ in which there is network inversion with ZrO_2 being the major

constituent instead of SiO_2 , are consistent with the SiO_4^{4-} molecular ion in the as-deposited films, and CPS into non-crystalline SiO_2 and crystalline ZrO_2 after the 900 °C anneal.

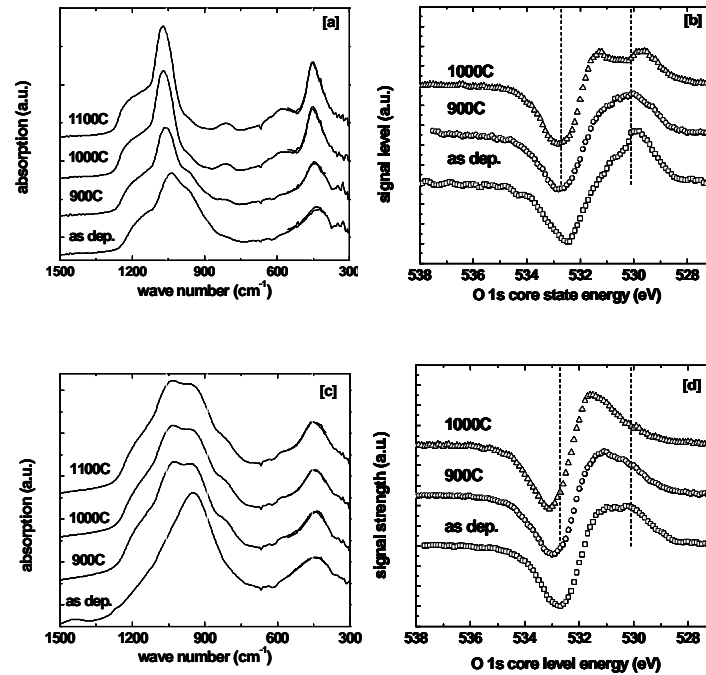


Fig. 7. (a) and (c) Infrared absorption spectra of as-deposited annealed thin film Zr Si oxynitride alloys, and (b) and (d) derivative x-ray photoelectron spectra for the same as - alloys. The approximate alloy constituent compositions for (a) and (b) are $(\text{SiO}_2)_{0.30}(\text{Si}_3\text{N}_4)_{0.40}(\text{ZrO}_2)_{0.30}$, and for (c) and (d), $(\text{SiO}_2)_{0.45}(\text{Si}_3\text{N}_4)_{0.45}(\text{ZrO}_2)_{0.1}$.

Figs. 7(a) and (c) display FTIR spectra for two pseudo-ternary $\text{Zr}(\text{Hf})\text{O}_2\text{-SiO}_2\text{-Si}_3\text{N}_4$ alloys, and Figs. 7(b) and (d) include derivative XPS O 1s core level spectra for these same alloys [28]. Spectra in Figs. 7(a) and (b) are those of an alloy with $\sim 8.8 \pm 1\%$ Si_3N_4 , $43.8 \pm 2\%$ SiO_2 and $\sim 47.4 \pm 2\%$ ZrO_2 . This alloy is in effect a Zr silicate alloy, with a relatively small concentration of Si_3N_4 . It displays qualitatively similar behavior to Zr silicate alloys. The FTIR and XPS spectra indicate CPS at annealing temperatures greater than 900 °C, as well as continuous changes in bonding at lower annealing temperatures. After the 900 °C anneal, there are non-crystalline SiO_2 features at $\sim 1050 \text{ cm}^{-1}$ and 800 cm^{-1} , and a nano-crystalline ZrO_2 feature at $\sim 450 \text{ cm}^{-1}$ in the FTIR spectrum. In the XPS there are two distinct spectral features after a 1000°C anneal, indicative, respectively of SiO_2 and ZrO_2 bonding. In addition, bonding changes at intermediate temperatures have been detected in studies of the soft x-ray absorption near edge structure (XANES) of these same alloy films [29]. These indicate relatively small bonding changes for annealing temperatures to about 750 °C with no evidence for CPS, and then a significantly larger change between 750 °C and 1000 °C, with unambiguous evidence for CPS.

Spectra in Figs. 7(c) and (d) are for an alloy with approximately equal concentrations of Si_3N_4 and SiO_2 , $\sim 45 \pm 1\%$ and a significantly reduced concentration of ZrO_2 , $10 \pm 2\%$. This alloy is in effect a Si oxynitride alloy with equal concentrations of SiO_2 and Si_3N_4 , and smaller ZrO_2 alloy fraction. After annealing, the FTIR indicates weak Si-O features which are more SiO_4^{4-} ion-like than SiO_2 network-like and a non-crystalline ZrO_2 feature. This is supported by derivative XPS that shows a single dominant feature at an energy that is significantly different from either non-crystalline SiO_2 or ZrO_2 , and closer in energy to the feature in as-deposited Zr silicate with 50% ZrO_2 , with no detectable evidence for CPS that includes SiO_2 and ZrO_2 .

The data presented above can be understood in terms of i) the general concepts of BCT, cast in terms of the average number of bonds/atom, n_c , and the average number of bonding constraints/atom, r_c [2,3], ii) the extension of BCT from continuous random networks (CRN) to disrupted networks with silicates being the prototypical examples [30], and iii) the competing factors

of bond energy (enthalpy) and configurational entropy that determine local atomic bonding, and morphology of multi-component oxides.

These three concepts are described in three theorems, and associated corollaries, and build on the ideas developed in Section 3.

I: A value of $r_c = 3.0$ equal to network dimensionality separates an alloy system into 2 regimes: (a) a floppy, or compliant regime for $r_c < 3$, (b) an over-constrained or stress-rigid for $r_c > 3$. $r_c \sim 2.5 n_c - 3$, with minor changes that reduce the bond-bending constraints at planar bonding sites such as N-atoms as in Si_3N_4 [2,3].

Corollary I(a): The density of bonding defects over-constrained networks is proportional to $[r_c - 3]^2$, where the bond-bending constraints are broken by bond-strain [31].

Corollary I(b): Bond-strain is relieved by formation of chemically-ordered intermediate phases [4,5], which can occur over limited ranges of alloy compositions, or at buried interfaces.

II: For silicates with ionic oxides, e.g., Na_2O and ZrO_2 , $n_{c,\text{metal}}$ is equal to the number of Pauling resonating single bonds/atom or chemical valence, 1 for Na and 4 for Zr, and not the actual coordination of 4 for Na, or 8 for Zr [30].

Corollary II(a): In low concentration silicates, where there is not significant network disruption, dative bonds are formed between the metal atoms, and non-bonding pairs on bridging O-atoms of the host SiO_2 CRN, restoring the bond-bending constraint of the O-atoms of an ideal SiO_2 CRN [32].

III: Network disruption is described in terms of the concentration of corner-shared $\text{SiO}_{4/2}$ tetrahedra. It is dependent on the concentration and primary valence of the ionic oxide additive(s) to the SiO_2 network [33].

Corollary III(a): The distribution of different corner-shared $\text{SiO}_{4/2}$ tetrahedra is statistical.

Fig. 8(a) describes network break-up in terms of shared corners/Si atom, C_s , versus metal oxide concentration; the oxide formula in one metal atom representation, e.g., Na_2O , is given by $\text{NaO}_{0.5}$. C_s equals $2[C_{\text{ox}} - C_{\text{MRB}}]$, C_{ox} is the oxygen atom concentration, and C_{MRB} is the concentration of resonating single bonds/metal atom. For $(\text{ZrO}_2)_x(\text{SiO}_2)_{1-x}$, $C_{\text{ox}} = 2$, and $C_{\text{MRB}} = 4x$, so that $C_s = 2[2 - 4x]$. For $x = 0$, $C_s = 4$, for the ideal corner-connected SiO_2 CRN, and for $C_s = 0.5$, $C_s = 0$ for the completely disrupted network of Zr^{4+} ions and SiO_4^{4-} molecular ions. $(\text{NaO}_{1/2})_{0.8}(\text{SiO}_2)_{0.2}$ corresponds to Na^{1+} ions and SiO^+ molecular ions, fully ionized limits for Ca^{2+} and Y^{3+} follow similar patterns [33].

The conclusions to be drawn from Fig. 8(a) are: i) metal atoms of ionic oxides disrupt or break-up the network connectivity, by converting bridging O-atoms in Si-O-Si arrangements to terminal ionic groups, SiO^+ ; ii) number of terminal groups equals the valence of metal ion, 1 for Na, 2 for Ca, 3 for Y and 4 for Zr; iii) the connectivity of the SiO_2 host network is defined by shared corners, C_s between $\text{SiO}_{4/2}$ units [33]; so that iv) $C_s = 4$ for a totally connected CNR network, and $C_s = 1.0$ completely disrupted network - a mixture of Si-O molecular ions and metal ions. Intermediate values of C_s give different degrees of network break-up. Alloys with metal atom concentrations greater than the x for which $C_s = 0$, are inverted, with the metal oxide phase dominant, and with an increasing concentration of O^{2-} ions as well Si-O molecular ions.

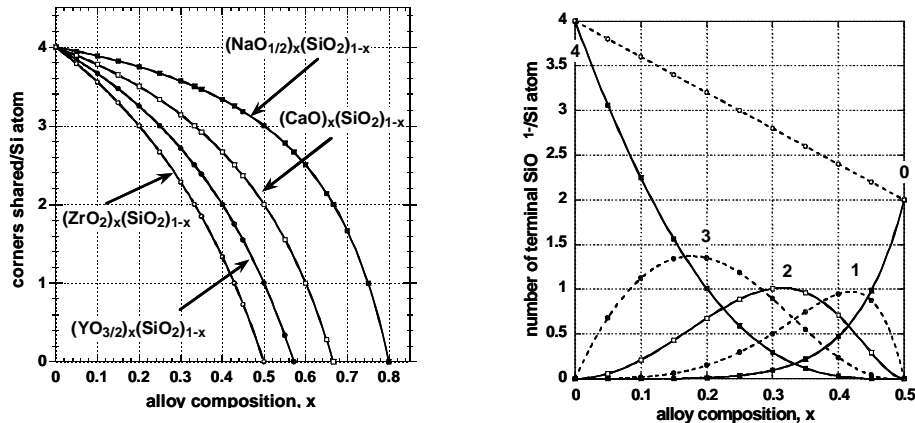


Fig. 8. (a) The mean-field concentration of corners, 0, 1, 2, 3, and 4, shared per tetrahedral $\text{SiO}_{4/2}$ arrangement for silicate alloys with +1, +2, +3 and +4 ionic oxide silicate additives. (b) The mean - field number of terminal SiO^+ groups per tetrahedron as a function of alloy composition.

Fig. 8(b) indicates the statistical distribution of $\text{SiO}_{4/2}$ units in ZrO_2 - SiO_2 alloys as a function of alloy composition, x , where 4, 3, 2, 1, or 0, is equal to C_s . Results presented in Figs. 6(a) and (b) for as-deposited films are consistent with Figs. 8(a) and (b). The low concentration alloy, $x = 0.23$, has a terminal SiO^{1-} group, the $\sim 950 \text{ cm}^{-1}$ FTIR feature, whilst, the higher concentration alloy, $x = 0.5$ has a SiO_4^{4-} spectral feature.

Since Zr(Hf) silicate alloys are i) over-constrained or stressed-rigid on deposition; i.e., $r_c > 3$, and ii) CPS into SiO_2 and Zr(Hf)O_2 is not blocked by a congruently-melting silicate phase. CPS is determined by kinetics, and increases as the temperature passes through $900 \text{ }^\circ\text{C}$, a temperature at which Si-O bond-breaking becomes increasing probable. Additionally, it is not possible to prepare Zr(Hf) silicate bulk glasses by quenching from a melt.

There are two ways to suppress CPS, and crystallization of the Zr(Hf)O_2 component completely. The first method has been by post-deposition nitridation of Zr or Hf silicate alloys, but the mechanism has not been explained, nor have conditions for complete suppression been identified [34]. The spectra in Figs. 7(a) and (b) provide the critical experimental data, and help to identify the mechanism that is an extension of the model pseudo-binary silicate alloys. Consider first $(\text{Si}_3\text{N}_4)_x(\text{SiO}_2)_{1-x}$ pseudo-binary alloys, where Fig. 9 gives the statistical distribution of Si atoms with different combinations of O and N atom nearest neighbors. The $x = 0.5$ composition is optimum for gate stack applications. At this composition the majority of the Si atoms, $\sim 42\%$, have 1 O and three N neighbors. There is also a chemically-ordered phase, Si_2ON_2 in which each Si has 3 N and 1 O neighbor.

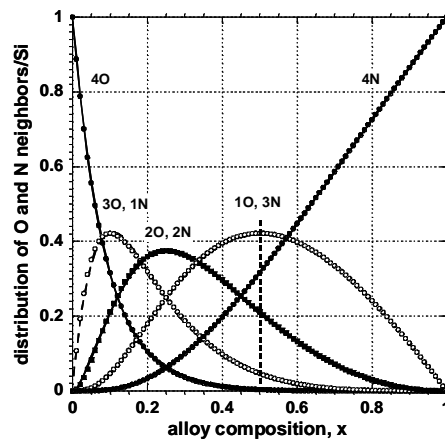


Fig. 9. The statistical distribution of Si atom neighbors in Si oxynitride alloys, $(\text{Si}_3\text{N}_4)_x(\text{SiO}_2)_{1-x}$, as a function of alloy composition. These groups include 4O, 3O and 1N, 2O and 2 N, 1O and 3N and 4N neighbors.

A pseudo-ternary with approximately equal concentrations Si_3N_4 and SiO_2 , $\sim 45\%$, and a significantly lower concentration of ZrO_2 , $\sim 10\%$, shows a bonding change by FTIR and XPS between the as-deposited state, and after a 1000 to 1100 $^\circ\text{C}$ anneal that is clearly not a chemical separation into SiO_2 and ZrO_2 . Based on the FTIR measurements, after annealing the local bonding can no longer be described as a Si oxynitride alloy with a small ZrO_2 alloy content. It is better described having a Si_3N_4 rich Si nitride alloy back-bone in which stress is relieved locally by chemical ordering at internal void surfaces which encapsulate Zr^{4+} ions by two Si-O^{1-} terminations/Si as in crystalline ZrSiO_4 . CPS into SiO_2 and ZrO_2 is hindered by the Si_3N_4 rich Si nitride alloy back-bone. In contrast, the lower Si_3N_4 content alloy, $\sim 10\%$, with approximately equal SiO_2 and ZrO_2 concentrations of $\sim 45\%$ displays CPS into SiO_2 and ZrO_2 because the Si_3N_4 content is insufficient to isolate the Zr^{4+} ions. These distinctions are supported by studies of other alloy compositions in the pseudo-ternary Zr(Hf)O_2 - SiO_2 - Si_3N_4 alloy systems.

6.1 Chalcogenide pseudo-silicate alloys

Pseudo-binary glasses and thin film alloys such $\text{Ag}_2\text{Se-As}_2\text{Se}_3$, and $\text{GeTe-Sb}_2\text{Te}_3$ are of interest for applications in photolithography, and read/write optical memories, respectively. BCT describes network strain, and its role in irreversible and/or reversible transitions that can be application enabling. These applications require either chemical stability, or intentional CPS. These

differences have been addressed above, focusing on applications as high-k dielectric thin films for advanced Si devices where atomically-engineered $\text{ZrO}_2\text{-SiO}_2\text{-Si}_3\text{N}_4$ alloys with low ZrO_2 concentrations are over-constrained, yet display self-organization, rather than CPS during annealing at temperatures required for process integration. As noted above, thin film chalcogenides can be i) optimally constrained CRNs with $n_c = 2.4$ and $r_c \sim 3$ as in $\text{As}_2\text{Se}_3\text{-As}_2\text{S}_3$, $\text{As}_2\text{S}(\text{Se})_3\text{-GeS}(\text{Se})_4$; ii) over constrained CRNs with $n_c > 2.5$, and with defect densities $\sim 10^{17}$ to 10^{19} cm^{-3} as in $\text{As}_2\text{S}(\text{S})_3\text{-GeS}(\text{Se})_2$, $\text{GeSe}(\text{Te})_2\text{-Sb}_2\text{Se}(\text{Te})_3$; or iii) disrupted by ionic additions as in $\text{Ag}(\text{Na,Cu})_2\text{Se-GeSe}_2$ or $\text{Ag}(\text{Na,Cu})_2\text{Se-As}_2\text{Se}_3$, with the extent of disruption being critical for specific applications. Specific examples addressed in this article include i) comparisons of network disruption based on Na_2O in SiO_2 as a point of reference for Na_2S in GeS_2 and As_2S_3 [35,36], and ii) the effects of bond strain in the over-constrained alloys, $\text{GeTe-Sb}_2\text{Te}_3$ and the like, that underpin their device functionality in DVD players [37,38].

Pseudo-binary alloys of SiO_2 and covalent or ionic metal oxides fall into two distinct classes differentiated by i) bond ionicity, and ii) bond-constraint counting. These distinctions are based on extension of BCT from i) continuous random networks, CRNs, e.g., solid solutions of SiO_2 and B_2O_3 , to ii) disrupted and modified silicate networks, SiO_2 mixed with ionic oxides (network additives) including Na_2O , CaO , Al_2O_3 and ZrO_2 [17]. CRN thin films formed by deposition and melt-quenched bulk glasses display the same local bonding and network structure, whereas for silicates, the situation is markedly different. Photo- or thermal-driven changes in thin film bonding that are device enabling are related to the state of bond-strain inherent in deposition kinetics, whereas properties of quenched-glasses may be different. The driving forces for these differences are qualitatively the same for i) SiO_2 -ionic oxide silicates, and ii) chalcogenide alloys where As/Ge sulfide/selenide CRNs are substituted for SiO_2 CRNs.

Pseudo-binary SiO_2 CRN glasses and thin films with covalent bonding obey the 8-N rule for coordination [17]. These oxides are either optimally constrained or floppy with mean-field bond coordinations, r_c of 2.4 or below. In contrast, and depending on the valence of metal, Na (+1), Ca (+2), Al (+3) and Zr (+4), thin film silicates vary systematically from floppy to over-constrained. This is reflected in the degree of network disruption and modification, and has been quantified accordingly. This has been introduced in the last section of this article in the context of trivalent and tetravalent transition metal oxide additives to an SiO_2 host CRN. The same approach is now applied for the first time to binary chalcogenide alloys, and the same systematics apply. It is therefore equally important to separate these alloys into different classes, based on bond-strain, combined with the degree of network disruption and/or modification.

Fig. 10 describes network break-up by the addition of the univalent metal sulfides (or selenides) such as $\text{Na}_2\text{S}(\text{Se})$, $\text{Ag}_2\text{S}(\text{Se})$ and $\text{Cu}_2\text{S}(\text{Se})$ into $\text{GeS}(\text{Se})_2$ and $\text{As}_2\text{S}(\text{Se})_3$ host CRNs. Values of C_s , corners shared per Ge(As) atom of 2(1.5) represent significantly disrupted networks, whilst values of 1(0.75) represent completely disrupted networks with no percolation of network conductivity. The model calculation for $\text{As}_2\text{S}(\text{Se})_3$ host CRN neglects S(Se) to As bonding, and which would require a significant charge redistribution as well.

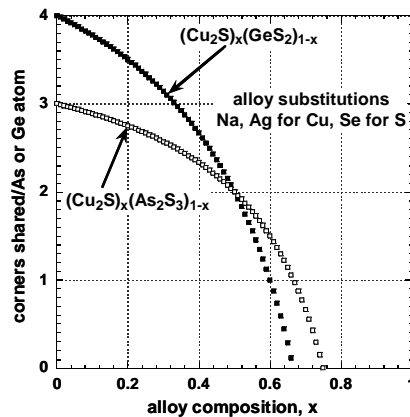


Fig. 10. The mean-field concentration of Ge atom corners, 0, 1, 2, 3, and 4, shared, C_s , per tetrahedral $\text{GeS}(\text{Se})_{4/2}$ arrangement for GeS_2 alloys with $\text{Cu}(\text{Na,Ag})_2\text{S}(\text{Se})$ ionic chalcogenide additives. The mean-field concentration of As atom corners, 0, 1, 2, and 3 shared, C_s , per pyramidal $\text{AsS}(\text{Se})_{3/2}$ arrangement for As_2S_3 alloys with $\text{Cu}(\text{Na,Ag})_2\text{S}(\text{Se})$ ionic chalcogenide additives. The calculation for the $\text{As}_2\text{S}(\text{Se})_3$ CRN host does not include the bonding of S(Se) atoms that can increase the coordination of As to four.

The $\text{As}_2\text{S}(\text{Se})_3$ host CRN is not stressed-rigid, and the same also applies at all alloy compositions. This observation is consistent with the experimental EXAFS studies on As-Cu-Se glasses [39,40]. In marked contrast, glass formation has not been observed in GeSe_2 - Ag_2Se alloys with up to ~20% Ag_2Se [35,36,41]. However, good glass formation has been found in this alloy system in two other composition regimes. The first includes alloys along the GeSe_4 - Ag_2Se join line with Ag_2Se compositions <20% Ag_2Se . This observation is consistent with the host CRN composition i) marking the onset of local bond-rigidity and ii) defining the beginning of an intermediate phase. The GeSe_4 - Ag_2Se alloys of interest are in a floppy regime, with $n_c \sim 2.5$, and $r_c \sim 0.2$. The second regime of good glass formation in the Ge-S(Se) system as at compositions close to $\text{Ge}_2\text{S}(\text{Se})_3$. This corresponds to a second intermediate phase regime; e.g., for Ag_2Se ~0.1 to 0.2, $r_c \sim 2.6$, and $n_c \sim 3.0$.

The non-crystalline ternary alloy $\text{Ge}_2\text{Sb}_2\text{Te}_5$ has been found to give reversible changes in optical transmission, and has become the preferred materials for use in DVD read-write (R-W) optical disk applications [37,38]. Changes in local bonding associated with optical laser light pulse produce changes in transmission that are read with a weaker laser pulse [37]. Studies have explored the properties of these non-crystalline thin films by extended x-ray absorption fine structure spectroscopy, EXAFS, and x-ray absorption near edge spectroscopy, XANES, and have determined the bonding coordination and nearest neighbor bond lengths in the as-deposited and laser written films [38]. Recent, and as yet unpublished XANES data presented in this paper confirm previously published results [42], but have additionally addressed the bond-coordination in greater detail. These results have provided the basis for an analysis of thin film bonding in the context of bond constraint theory, BCT, which provides a new interpretation of the local atomic structure in the amorphous phase. This approach has been extended to other alloy compositions that are also of technological interest including the compositions, GeSb_2Te_4 and GeSb_4Te_7 that also fall on a tie-line between GeTe and Sb_2Te_3 in a compositional phase diagram. An analysis of bonding in the context of BCT, and the interpretation of our XANES data has raised significant issues relative to the short range order in non-crystalline films, and this tie-line representation [37,38].

Based on the new XANES results, bonding changes in optical memory applications have been referenced to an amorphous state including Ge_2Te_3 and Sb_2Te_3 units as well as a small fraction of three-fold coordinated Te atoms. Ge has 3.9 ± 0.15 nearest neighbors: 3.3 ± 0.1 Te and 0.6 ± 0.1 Ge. In this model, three-fold Te atoms act as nucleating sites for the transition from an amorphous to nanocrystalline state, and changes in transmissivity are shown to scale directly with the fraction of these nucleation sites. The transition is less abrupt in alloys with a higher fraction of 4-fold Sb nucleation sites [37].

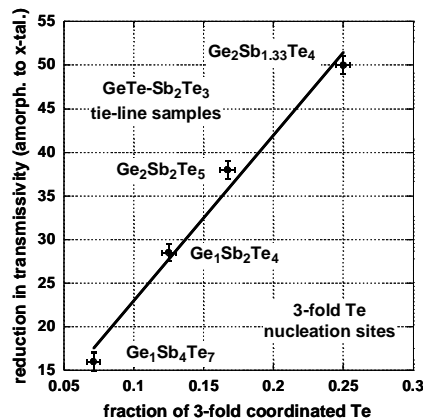


Fig. 11. Reduction of transmissivity as a function of the fraction of three-fold coordinated Te atoms in the amorphous to crystalline transition in "GST" alloys along the tie-line from GeTe to Sb_2Te_3 .

Based on the new XANES studies, bond-counting algorithms have been developed that apply to continuous random networks as well as non-crystalline solids in which the coordination is greater than the 8-N rule. The mean coordination, r_c , for $\text{Ge}_2\text{Sb}_2\text{Te}_5$ is 2.93. Based on the GeTe - Sb_2Te_3 tie-line model of Ref. 38, this composition is stressed-rigid with a mean-field number of bond-constraints/atom, $n_c = \sim 4.3$. An alternative model associated with a change in the local bonding of Ge from a $\text{Ge-Te}_{4/2}$ arrangement of Ge-Te, to a $\text{Ge-Ge-Te}_{3/2}$ arrangement of Ge_2Te_3 gives a

significant reduction of n_c . This composition is stressed-rigid in the alternative model, but with a mean-field number of bond-constraints/atom, $n_c = \sim 3.4$. This includes a reduction of Ge atom bond-bending constraints associated with a change in symmetry from Ge-Te_{4/2} to a Ge-Ge-Te_{3/2} arrangement. In this model, $r_{c,eff}$ is reduced to a value of 2.54, accounting for the ease of glass formation. In the context of the new bonding model, other GST alloys considered for optical memory applications, GeSb₂Te₄ and GeSb₄Te₇, are also stressed-rigid, but reduced values of $r_{c,eff}$. $r_{c,eff}$ values of 2.7 and 2.5, with n_c values ~ 3.7 and ~ 3.3 apply to GeSb₂Te₄ and GeSb₄Te₇, respectively. The three alloys discussed above contain significant concentrations of three-fold Te, ranging from 16.7% for Ge₂Sb₂Te₅ to 12.5% and 7.1% for GeSb₂Te₄ and GeSb₄Te₇, respectively.

The most important result of the new model is addressed in Fig. 11 that contains a plot of the normalized reduction in transmittivity as a function of the fraction of three fold Te bonding sites. This plot for the amorphous to crystalline transition as determined from the results presented in Ref. 37, and is consistent with a model in which these sites act as nucleation centers for this transition.

The stressed-rigid nature of the GST films in the plot suggests that bonding changes induced by the write pulse relieve bond-stress by converting the bond-strain energy into increases in the coordination for both Ge and Te. The Ge coordination increases from 4 to 6 neighbors, and the Te coordination and bond-lengths change accordingly. In effect the transition trades configuration entropy in the amorphous state for an increase in bond enthalpy in the crystalline state.

The model proposed above is being tested by performing XANES studies for GST alloy compositions that lie on the tie line from Sb to GeSb₂Te₄. Determination of the number of Ge-Te, Sb-Te and Ge-Ge neighbors, as well as the number of bonds/Te and Sb atoms are being made. These will then be correlated with optical transmissivity results of Ref. 37. These samples contain Sb-Sb bonds as well, and it is important to test the scaling relationship between these homopolar bond concentrations, and the crystallization kinetics.

7. Self-organization: A pathway to device applications

Thin films prepared by plasma CVD at 300 °C are addressed with respect to this issue. It will be demonstrated that in Si_xN_yH_{1-x-y} alloys self-organization occurs during deposition [43], but in (SiO₂)_x(Si₃N₄)_y(ZrO₂)_{1-x-y} it occurs during or after high-temperature anneals at temperatures $\geq 900^\circ\text{C}$ [28]. Thin films in the self-organized intermediate phases are used as gate dielectrics in a-Si:H TFTs and crystalline (c-) Si FETs so that it is important to address this issue.

In plasma-deposited a-Si_xN_yH_{1-x-y} alloys, the source gas ratio, $R = \text{NH}_3/\text{SiH}_4$. $R = 2-7$ gives sub-nitride films with $y/x < 1.3$ and H in Si-H groups, $R = 12-15$ gives films with $y/x > 1.6$ and H in Si-NH₂ groups. There is a narrow range of gas ratios, $R = 10 \pm 0.5$, with $y/x \sim 1.5 \pm 0.05$. This regime defines an intermediate phase between a floppy regime for $R > 11$, and stressed-rigid regime for $R < 9.5$. Minimization of bonding defects in this intermediate phase has been detected by the variation of TFT channel mobility, μ , with R . $\mu < 0.5 \text{ cm}^2\text{V}^{-1}\text{cm}^{-1}$ for $R < 8$ and $R > 11$, but for R in a narrow regime between ~ 9.5 and $1 \text{ cm}^2\text{V}^{-1}\text{cm}^{-1}$, for an alloy with a composition $\sim \text{Si}_{0.3}\text{N}_{0.4}\text{H}_{0.3}$. In this alloy $n_c = 2.7$, and the average number of bonding constraints/atom, $r_c = 3.0 \pm 0.1$. This value of r_c is an indicator of a self-organization that suppresses percolation of network rigidity, thereby reducing defects that trap channel electrons during TFT operation. The plot in Fig. 12 represents the first electrical detection of an intermediate phase.

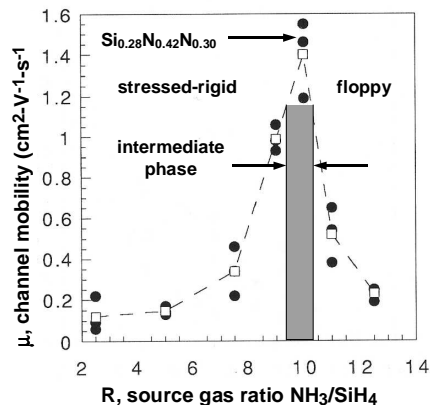


Fig. 12. Channel mobility of electrons in a-Si:H TFTs as a function of the source gas ratio, $R = \text{NH}_3/\text{SiH}_4$. Based on determinations of H, Si and N atom concentrations as function of, the diagram includes the identification of stressed-rigid, intermediate phase and floppy SiNH concentrations.

Similar behavior occurs in $(\text{SiO}_2)_x(\text{Si}_3\text{N}_4)_y(\text{ZrO}_2)_{1-x-y}$ alloys deposited at 300°C and then annealed at high temperatures $\geq 900^\circ\text{C}$. Alloys with approximately equal concentrations of SiO_2 and ZrO_2 ($x \sim 1-x-y$), but with smaller concentrations of Si_3N_4 , $y < x$, display chemical phase separation (CPS) into non-crystalline (nc-) SiO_2 and crystalline ZrO_2 after annealing to 900°C , whereas alloys with approximately equal concentrations of SiO_2 and Si_3N_4 , $x \sim y$, with $x > 35\%$, display spectroscopic evidence for bonding changes for annealing temperatures up to 900°C , but the absence of CPS into SiO_2 and ZrO_2 for annealing at temperatures $> 900^\circ\text{C}$. These as-deposited films have mean-field values of $n_c > 3.1$ and $r_c > 3.85$. After 900°C annealing, alloys display chemical ordering with non-crystalline (n-c) Zr silicate groups encapsulated within a non-crystalline Si_3N_4 back-bone with $n_c = 2.77$ and $r_c = 3.2 \pm 0.1$. These values of n_c are close to those, $r_c = 3.0$ to 3.3 , of glasses and films within the intermediate phase of $\text{Ge}_x\text{Se}_{1-x}$ where $x \sim 0.2$. Finally, it is significant to note that concurrent with CPS in the low Si_3N_4 content films, there is a release of N at temperatures at which the CPS occurs. This has been detected by XAS, as well as XPS and FTIR.

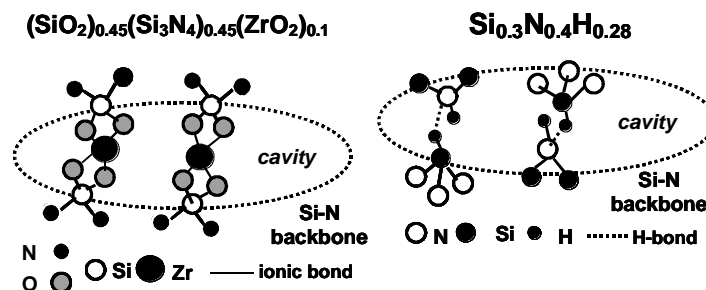


Fig. 13. Schematic representation of the bonding of Zr^{4+} ions in a "cavity" region of the Si-N backbone structure. Ionic bonds are formed with two terminal SiO^+ states that are at the boundary of the cavity. Four additional bonds are made to other terminal O atom groups reducing the bond order to 0.5, and increasing the O atom coordination to three as in stoichiometric ZrSiO_4 .

The bonding of terminal O-atoms in the $(\text{SiO}_2)_{0.45}(\text{Si}_3\text{N}_4)_{0.45}(\text{ZrO}_2)_{0.1}$ alloys, and terminal Si-N-H and Si-H groups in the $\text{Si}_{0.3}\text{N}_{0.4}\text{H}_{0.28}$ alloys in the intermediate phase regime are responsible for the low values of r_c . A schematic representation of this bonding is displayed in Fig. 13. Low r_c is the result of functionally equivalent chemical self-organizations that prevent percolation of network stress, thereby avoiding formation of defects that would degrade TFT and FET performance.

8. Conclusions

The ab initio calculations highlighted in this article were first applied to SiO_2 , using a central cluster that includes the Si-O, and Si-Si and O-O bond lengths (or equivalently the Si-O-Si and O-Si-O bond angles) obtained from diffraction studies. The Si atoms at the boundaries of these central clusters were terminated by O atoms attached to pseudo-Si atoms or H-atoms. Similar clusters were constructed for As- and Ge-chalcogenides as well. After configuration interaction refinements these calculations gave an excellent description of i) the local atomic structure, ii) the infrared effective charges that are associated with the normal mode motions of the O and chalcogen atoms, and ii) band edge optical transitions before, and after light-soaking.

The effects of more distant neighbors, or equivalently the coupling between the central clusters and the CRNs in which they have been embedded has been described in terms of bond constraint theory. BCT. This formalism is based on the number of bonds/atom or mean-field coordination, n_c , and the number of valence force field bonding constraints/atom, r_c . This formulation provides a basis for dividing an alloy system, e.g., $\text{Ge}_x\text{Se}_{1-x}$ into three distinct regimes with different properties: i) a floppy regime, in which $r_c < 3$, ii) a stress free or intermediate phase regime in which $r_c \sim 3$, and iii) a stressed-rigid or over constrained regime in which $r_c > 3$. One of the most significant results of this approach has been the detection of the intermediate phase regime. This regime is bounded by two transitions: i) the first marks the onset of mean-field bond rigidity, and the ii) the second the percolation of bond-strain or rigidity throughout the entire network. Percolation of strain in the intermediate phase regime is prevented by chemical self-organization

into non-statistical bonding groups.

One of the most important contributions of this paper is related to the application of BCT for i) describing significant features in the IR spectra, and vibrational density of states determined by inelastic neutron scattering, that are not associated with oxygen or chalcogen normal mode motions, and ii) distinguishing between elastic and inelastic photo-structural changes following light-soaking. A second contribution is related to the extension of BCT to silicate and pseudo-silicate chalcogenides in which there significant network disruption and modification associated with the incorporation of ionic alloy constituents.

The second contribution quantifies network disruption in silicates and chalcogenide analogues, and then applies this approach to several important classes of thin film materials, including chalcogenides alloys for photolithographic and reversible optical memory applications, and hydrogenated silicon nitride and Zr Si oxynitride films for gate dielectric applications in amorphous Si TFTs and crystalline Si and other semiconductor FETs. In all of these applications, intermediate phases play a significant role in the functionality required for the specific applications.

Acknowledgements

The author acknowledges and on-going collaborations with Jim Phillips, formerly of Bell Labs, and currently at Rutgers University, Punit Boolchand of the University of Cincinnati, and Mike Thorpe, formerly of Michigan State University, and currently at Arizona State University. The author acknowledges research support from the Office of Naval Research, and the Semiconductor Research Corporation. Finally, the research results reflect the contributions of a significant number of Professor Lucovsky's Ph.D. students and post doctoral fellows, who are identified in the references.

References

- [1] J. L. Whitten, Y. Zhang, M. Menon, G. Lucovsky, *J. Vac. Sci. Technol.* **B 20**, 1710 (2002).
- [2] J. C. Phillips, *J. Non-Cryst. Solids* **34**, 153 (1979).
- [3] J. C. Phillips, *J. Non-Cryst. Solids* **43**, 37 (1981).
- [4] P. Boolchand, in *Insulating and Semiconducting Glasses*, ed. P. Boolchand (World Scientific, Singapore, 2000), p. 191.
- [5] P. Boolchand, D. G. Georgiev, M. Micoulaut, *J. Optoelectron. Adv. Mater.* **4**, 823 (2002).
- [6] R. L. Mozzi, B. E. Warren, *J. Appl. Cryst.* **2**, 164 (1969).
- [7] R. J. Bell, P. Dean, *Phil. Mag.* **25**, 1381 (1972).
- [8] J.L. Robertson, S. C. Moss, *J. Non-Cryst. Solids* **106**, 330 (1988).
- [9] J. Neufeind, K. -D. Liss, *Bur Bunsen Phys Chem* **100**, 1341 (1996).
- [10] G. Lucovsky, T. Mowrer, L. S. Sremaniak, J. L Whitten, *J. Non-Cryst. Solids* **338-340**, 155 (2004).
- [11] M. O'Keefe, B. G. Hyde, *Acta Crystallogr.* **B 34**, 27 (1978).
- [12] E. Burstein, M. H. Brodsky, G. Lucovsky, *Int. J. Quantum Chem.* **1s**, 759 (1967).
- [13] F.L. Galeener, G. Lucovsky, *Phys. Rev. Lett.* **37**, 1474 (1976).
- [14] F.L. Galeener, G. Lucovsky, R. H. Geils, *Solid State Commun.* **25**, 405 (1978).
- [15] Y. Zhang, Ph. D. Dissertation, Department of Physics, North Carolina State University (2004).
- [16] G. Lucovsky, et al., *IEEE Trans. Dev. Materials Reliability* (2005), in press.
- [17] R. Zallen, *The Physics of Amorphous Solids* (John Wiley & Sons, New York, 1983), Chapter 2.
- [18] M.F. Thorpe, et al., *J. Non-Cryst. Solids* **266**, 859 (2000).
- [19] G.B. Rayner, D. Kang, G. Lucovsky, *J. Vac. Sci. Technol.* **B 21**, 1783 (2003).
- [20] G. Lucovsky, C.K. Wong, W.B. Pollard, *J. Non-Cryst. Solids* **59 & 60**, 839 (1983).
- [21] K. Tanaka, in *Structure and Excitations in Amorphous Solids*, ed. by G. Lucovsky and F.L. Galeener (American Institute of Physics, New York, 1976), p. 148.
- [22] S.R. Elliott, *J. Non-Cryst. Solids* **81**, 71 (1986).
- [23] H. Fritzsche, in *Insulating and Semiconducting Glasses*, Ed. by P. Boolchand (World Scientific, Singapore, 2000), p. 653.
- [24] T. Morwrer, G. Lucovsky, L.S. Sremaniak, J.L. Whitten, *J. Non-Cryst. Solids* **338-340**, 543 (2004).

- [25] J.M. Lee, M.A. Paesler, D.E. Sayers, A Fontaine, *J. Non-Cryst. Solids* **123**, 295 (1990).
- [26] W. Pontuschka, P.C. Taylor, *Solid State Commun.* **38**, 573 (1981).
- [27] G.B. Rayner, D. Kang, G. Lucovsky, *J. Non-Cryst. Solids* **338-340**, 151 (2004).
- [28] G. Lucovsky, in *Topics in Applied Physics*, Springer-Verlag (2005) in press.
- [29] J. Luning, G. Lucovsky, B.S. Ju, unpublished.
- [30] R. Kerner, J.C. Phillips, *Solid State Commun.* **117**, 47 (2001).
- [31] G. Lucovsky, Y. Wu, H. Niimi, V. Misra, J.C. Phillips, *Appl. Phys. Lett.* **74**, 2005 (1999).
- [32] G.B. Rayner, D. Kang, Y. Zhang, J.L. Whitten, G. Lucovsky, *J. Vac. Sci. Technol.* **B 20**, 1748 (2002).
- [33] A.K. Varshneya, *Fundamentals of Inorganic Glasses* (Academic Press, Boston, 1994), Chap. 5.
- [34] M.R. Visokay et al., *Appl. Phys. Lett.* **80**, 3183 (2002).
- [35] A. Feltz, *Amorphe and Glasartige Anorganische Kestkorper*, (Academic Press, Berlin 1983).
- [36] Y. Wang et al., *J. Phys. Condens. Mater.* **14**, 1573 (2003).
- [37] N. Yamada, T. Matsunaga, *J. Appl. Phys.* **69**, 2849 (1991).
- [38] A. Kolobov et al., *Nature* **3**, 705 (2004).
- [39] S.H. Hunter, A. Bienenstock, T.M. Hayes, in *Proc. 7th Intern. Conf. on Amorphous and Liquid Semiconductors*, Edinburgh, ed. W.E. Spear (Centre for Industrial Consultancy and Liason, University of Edinburgh, 1977), p. 78.
- [40] S. Laderman, A. Bienenstock, K.S. Laing, *Solar Energy Materials* **8**, 15 (1983).
- [41] M. Mitkova, in *Insulating and Semiconducting Glasses*, ed. P. Boolchand (World Scientific, Singapore, 2000), p. 813.
- [42] D.A. Baker, M.A. Paesler, G. Lucovsky, P.C. Taylor, unpublished.
- [43] G. Lucovsky and J.C. Phillips, *J. Non-Cryst. Solids* **227**, 1221 (1998).